Low Energy electron attachment to SF_6 at sub-meV resolution using a new, tunable laser photoelectron method

P-T. Howe[1], A. Kortyna[2], M. Darrach[1], and A. Chutjian[1]

[1]*Jet Propulsion Laboratory, California Institute of Technology, Pasadena, CA 91009, USA*

[2]*Department of Physics and Astronomy, Colby College, Waterville, ME 04901, USA*

Abstract

Electron attachment to sulfur hexafluoride is studied using a new photoelectron source of ultralow energy electrons with sub-millielectron volt resolution. Vacuum ultraviolet laser radiation produced through nonlinear optical techniques is used to photoionize xenon at and above its $^2P^o_{1/2}$ ionization limit. The resulting photoelectrons interact with sulfur hexafluoride admixed to the xenon. The electron energy is continuously scanned from 0 to 127 meV, with a resolution of 0.1 meV at threshold. Computational modeling indicates that the attachment cross section is well described by the Wigner threshold law at electron energies less than about 5 meV. Data at higher energies are best described by the Wigner *s*-wave form, or by a Klots form with small β. Cusps are clearly observed at the ω_6, ω_1, and ω_3 vibrational modes of SF_6. While the ω_1 and ω_3 cusps have their maxima at the spectroscopic energies of 97.1, and 117.6 meV, respectively; the ω_6 cusp has its maximum at 46 meV, nearly three meV *higher* than its spectroscopic value of 43.2 ± 0.4 meV. Possible explanations are considered, such as a low-*l* angular-momentum barrier, or an overtone mode of SF_6 excited by the collision. The definitive cause of this shift is not understood.

PACS Classification No.: 34.80.Ht 39.90.+d 07.77.-n

I. INTRODUCTION

Sulfur hexafluoride (SF_6) has become a classic molecule for the study of electron attachment at ultralow electron energies. The attachment of low-energy electrons to SF_6 results in formation of a metastable negative ion by the process,

$$SF_6 + e^- \rightarrow SF_6^- . \qquad (1)$$

The large peak in cross section in the vicinity of zero electron energy has a width limited only by the experimental resolution, hence pointing to an infinitely narrow cross section at threshold. Interest in this system also stems from practical considerations. Foremost is the need to better understand its properties (arising from its large thermal-energy attachment cross section and a high ionization potential) which make it an excellent gaseous insulator [1]. Its large zero energy attachment peak also makes SF_6 a useful tool in the selective detection of low energy electrons, with applications including the calibration of low energy electron beams [2], measurement of threshold photoelectron spectra of molecules (**T**hreshold **P**hotoelectron **S**pectroscopy by **E**lectron **A**ttachment, or TPSA) [3], and the study of SF_6 interaction with high-Rydberg atoms [4].

The electron attachment properties of SF_6 have been extensively studied in several experimental approaches using thermionically-generated electron beams, electron swarms, and flowing afterglows. Due to their relatively broad energy resolutions, typically on the order of 20-100 meV, these techniques cannot probe the threshold electron scattering region. A review of experimental approaches is given in Ref. [5], with extensive summaries and data for SF_6 given in Ref. [1].

Recent calculational and theoretical studies include the modeling of the attachment process in SF_6 [6], $CFC\ell_3$, and $CC\ell_4$ [7]. Here, use was made of an adiabatic approximation to the exact expressions for resonant attachment [5,8]. Theoretical work using non-adiabatic nuclear coupling [9], and quasiclassical resonant R-matrix theory [10] have aided in the understanding of the s-wave

attachment, vibrational cusps, and vibrational Feshbach resonances reported here and elsewhere [11-14].

Experimentally, the introduction of two optical techniques for the study of threshold electron attachment behavior has yielded significantly higher resolution with which to probe the *s*-wave attachment phenomenon closer to zero energy. These techniques are (1) charge-exchange involving optically-prepared Rydberg atoms, and (2) attachment of free electrons produced by photoionization. The charge-exchange technique employs narrow linewidth lasers to prepare rare gas atoms in high-lying Rydberg states Ry_{nl} (principal quantum number n and orbital quantum number l). The highly excited electrons behave as quasi-free particles, with an energy given by the root-mean-square of the electron's kinetic energy. The subsequent charge-exchange collision,

$$SF_6 + Ry_{nl} \rightarrow SF_6^- + Ry^+ \qquad (2)$$

leads to the formation of negative ions. The electron energy is determined by the initial *nl* Rydberg level. These collisional ionization experiments have been used to study electron attachment between 0.004 meV and 10 meV [15-17], although the energy resolution is limited by the relatively large velocity distributions inherent to the optically-accessible, low-l states. Also, one is confined to taking discrete steps in energy, as given by the spacing of Rydberg levels. One would often like to take finer, equally-spaced energy steps, for example to bring out the vibrational features discussed herein (Sec. IV.B)

The second optical technique employs a variation on the TPSA method. TPSA took advantage of the *s*-wave attachment cross section of SF_6 (and other species) to selectively produce their negative ions whenever low-energy electrons were present: the attacher was used as a "detector." TPSA was applied to the measurement of threshold photoionization spectra of molecules (hence its name). Subsequently, use of the TPSA method was essentially inverted by (a) first producing photoelectrons of well-defined energy and width, (b) then using *these* electrons to study the attachment properties of the molecular target itself. Chutjian and coworkers [18-21] used a vacuum ultraviolet (VUV) monochromator to disperse the helium Hopfield continuum generated by a high-pressure helium

discharge. The wavelength-selected VUV was used to photoionize rare gas atoms (argon or xenon) admixed with the molecular target. The collision energy was scanned by sweeping the grating of the VUV monochromator. An instrument resolution of 4-6 meV was obtained during scattering experiments, limited by their level of stray fields at the target center.

The free-electron method was significantly refined by Hotop and coworkers [22-25], who used a narrow-band dye laser as a tunable ionization source. Both a multistep ionization scheme (electron-impact excitation of metastable Ar* level, followed by laser-ionization to just below or above $^2P_{3/2}$ continuum) and a single-step scheme (direct laser-ionization of K atoms to the continuum) have been employed. Klar *et al.* achieved electron energy resolutions as low as 20 μeV at threshold, and measured relative electron attachment scattering cross sections of SF_6 over the approximate range of 0 - 200 meV.

In the present work, a new experimental laser-ionization technique is used to generate the ultralow-energy electrons at high resolution. A simpler, single-step, rare-gas ionization (as in the TPSA technique) is used, but the source of ionization is now tunable 92 nm laser radiation produced from a 1064 nm Nd:YAG laser by (a) doubling, (b) mixing with a frequency-shifted 573.6 nm output of a dye laser, and (c) frequency tripling *in vacuo* to obtain 92 nm. Using this, we report herein the energy dependence of the attachment process of Eq. (1), measured at an instrumental resolution of 0.1-0.5 meV over the range 0-130 meV. By comparing our data to a computational model, find that below 5 meV the attachment cross section is better described by the Wigner *s*-wave behavior [26] rather than by a parametrized form [27]. We also observe clear cusps in the attachment cross section characteristic of the opening of new vibrational excitation channels in the ω_6, ω_1, and ω_3 vibrational modes of SF_6 at 43.1, 97.1, and 117.6 meV, respectively.

II. EXPERIMENTAL ARRANGEMENT

The photoelectron attachment apparatus used in the present study was described in part in Ref. [28] for photoionization measurements in Xe. A schematic diagram is given in Fig. 1. The present approach involves the production of tunable, laser-derived VUV radiation to photoionize xenon atoms that have been admixed to the molecular target (here, SF_6). As the laser energy is scanned above the Xe $^2P^o_{1/2}$ ionization limit (its second ionization limit) low-energy electrons are generated. The energy of the photoelectrons is the difference between the laser energy and the $^2P^o_{1/2}$ ionization limit. The energy width of the photoelectrons is set by the laser bandwidth, Doppler broadening, and levels of stray fields in the collision region. These broadening effects are usually confined to a level less than 0.1 meV at threshold.

As low-energy electrons are generated they attach to the admixed SF_6 to form SF_6^-. The energy dependence of the attachment process is studied by continuously scanning the laser energy and recording the mass-resolved SF_6^- signal.

The $^2P^o_{1/2}$ ionization limit is chosen to differentiate the attachment signal from the competing negative-ion formation by charge-exchange collisions with highly excited Rydberg atoms that are formed just below the $^2P^o_{1/2}$ threshold. Since the $^2P^o_{1/2}$ threshold is embedded in the $^2P^o_{3/2}$ continuum, its Rydberg levels are short-lived due to autoionization. Hence the competing Rydberg-attachment signal is greatly reduced, though not eliminated. The issue of the charge-exchange signal is addressed in Sec. IV. The critical components of the apparatus are the VUV laser system, the attachment region, and the ion detection instrumentation. These are now described in detail.

The tunable VUV photoionization system is based on a Nd:YAG pumped pulse-dye laser. The second harmonic of an etalon-narrowed, 10 Hz, Q-switched Nd:YAG laser (0.1 cm^{-1} linewidth) pumps the dye laser. The dye is a mixture of Rhodium R590 and R610 optimized to produce tunable radiation near 575 nm (0.08 cm^{-1} linewidth). Residual infrared radiation after the first up-conversion of the Nd:YAG fundamental is frequency-doubled a second time and mixed in a KDP* crystal with the dye laser

output to produce 4-6 mJ of tunable UV radiation at about 276 nm, with a linewidth of 0.2 cm^{-1}.

VUV radiation is produced by frequency-tripling the UV laser beam in a pulsed, free-jet of Xe located in a differentially-pumped vacuum chamber. A 500 mm quartz lens focuses the UV laser beam into a pulsed Xe beam produced by a piezoelectric-actuated pulsed valve. The VUV radiation has a wavelength range 91 nm $\leq \lambda \leq$ 92.5 nm. Its linewidth is approximately 0.3 cm^{-1} (photoelectron energy resolution of 70 μeV). The VUV wavelength is controlled by adjusting the dye laser wavelength. Xenon is also used as the *tripling* medium at **T** (Fig. 1) [in addition to its use as the *electron source* at **G**] because it has a markedly uniform third-order susceptibility over the wavelength range. Settings of other parameters for third-harmonic generation (*e.g.*, pulsed valve backing pressure, nozzle-to-focal-point distance, and timing between the pulsed-valve trigger and laser trigger) are described in Ref. [28].

After interacting with the frequency-tripling jet the laser beam contains two wavelength components: the fundamental UV and the third-harmonic VUV. Neither Xe nor SF_6 have transitions near 276 nm, so the Xe-SF_6 target beam is transparent to the UV component. Nevertheless, we conducted attachment experiments using two configurations to verify this. The first used a straight-through configuration where both the UV and VUV light passed directly into the attachment region. The second used a pair of glancing incident dichroic beam splitters to separate the VUV from the UV [29]. Both beam splitters were quartz wedges oriented such that the surface normals are turned 70° from the beam. Each beam splitter also had an antireflective coating for the UV, allowing for more than 99% transmission at 276 nm, while having a reflectivity of about 50% at 92 nm. After interacting with the beam splitters, the laser beam overall maintained a collinear direction of propagation, but its 276 nm/92 nm intensity ratio was reduced by a factor 5×10^{-4}.

Data taken in the linear configuration were in good agreement with data taken in the collinear configuration. Identical features and behaviors were observed, indicating that indeed the UV radiation did not interact with the target beam in any significant way. However, these tests did reveal an important

source of negative-ion background which could be reduced, but not eliminated by use of the dichroic mirrors. It was understood in terms Rayleigh scattering of the 276 nm radiation onto the target-chamber surfaces (see Sec. III).

The VUV beam intersects the target beam to form a collision region roughly cubic in volume, and measuring about 4 mm per side. The target beam is produced by a second piezoelectric-actuated pulsed valve backed by mixture of 90% Xe and 10% SF_6 at 1 atm pressure. Electrons produced by Xe photoionization have a kinetic energy ϵ given by $\epsilon = hc/\lambda - T_{1/2}$. Here, h is Planck's constant (eV s), c is the speed of light (cm s^{-1}), λ is the VUV wavelength (cm), and $T_{1/2}$ is the energy of the Xe $^2P^o_{1/2}$ ionization limit (13.43637 ± 0.00002 eV [28,30]). The electron kinetic energy is changed by scanning the UV wavelength, which in turn varies λ. Calibration of λ is accomplished by comparing the Xe $nd'[3/2]^o_1$ autoionizing resonances measured in the positive ion spectra converging on the $^2P^o_{1/2}$ threshold (see [28] for details), and comparing their positions to those reported in Ref. [30]. The calibration error in ϵ was 0.1 meV.

Upon ionization free photoelectrons attach to the SF_6 in the target beam [Eq. (1)]. To within present experimental error, the Xe photoionization cross section was found to be constant over the wavelength range covered in this investigation, as was verified by observing the Xe^+ production rate as a function of λ, both here and in Ref. [28]. More accurate photoabsorption data show about a 0.5% decrease in the Xe ionization cross section in the present wavelength range [31]. No correction for the wavelength dependence of the photoionization cross section was applied.

We note that there are *two* ionization channels available when the VUV photon energy exceeds $T_{1/2}$. One channel ionizes to the desired Xe^+ $^2P^o_{1/2}$ state, while the other channel ionizes to the lower-lying Xe^+ $^2P^o_{3/2}$ state. Photoelectrons produced by the $^2P^o_{3/2}$ channel, however, could not be detected in the attachment signal due to their relatively large kinetic energies ($\epsilon \geq 1.306$ eV). This is because the attachment cross section falls by four orders of magnitude between 80 meV and 500 meV, and is

expected to be negligible for $\epsilon \geq$ 1.3 eV.

Approximately 5 μs after the VUV laser pulse passes through the attachment region, a pulsed electric field extracts the newly formed negative ions into an ion-lens system which focuses them and into a quadrupole mass spectrometer. Mass-analyzed SF_6^- is detected with a channel-type particle multiplier whose output is discriminated, amplified, and shaped. Data are accumulated in a multichannel scaler as a function of VUV wavelength. It was verified that the ion production rate follows a cubic dependence on the UV (276 nm) laser power. This is accounted for by normalizing the signal to the UV laser power, which is monitored during data collection by a volume absorber thermopile.

III. MITIGATION OF STRAY ELECTRIC AND MAGNETIC FIELDS

Stray electric and magnetic fields must be minimized in the electron-molecule attachment region, since these fields lead to poor energy resolution and other anomalies in the attachment signal. A nonzero magnetic field, for example, will cause cyclotron motion of the photoelectrons, leading to a larger scattering length and hence spuriously larger attachment signal at low scattering energies. (By example, a 1 meV electron subject to a 0.5 G field has a 2 mm Larmor radius, comparable to the detector view region.) To minimize spiraling we placed a high-permeability μ-metal shield around the attachment region, reducing the magnetic field to less than 10 mG. The Larmor radius for a 0.1 meV electron at this field intensity is about 30 mm, significantly larger than the dimensions of our attachment region. One therefore would not expect a meaningful increase in electron pathlength at energies greater than 0.1 meV.

Reduction of stray electric fields is also critical to achieving high resolution. A potential difference of V_0 across the attachment region will limit the ultimate energy resolution to approximately eV_0. Initially, electric fields were reduced with a box arrangement of electrodes modeled on the design of Frey *et al.* [32]. Three pair of chemically-pure Ti plates formed a box with inside dimensions 3 cm

× 3 cm × 2.5 cm. Bias voltages were applied across the sets of parallel faces to cancel stray fields in the attachment region. The voltage resolution on the biases was less than 1 mV, and each bias was actively filtered to reduce ripple to below 1 mV.

In the course of the earlier measurements it was found from extensive tests that low-energy electrons were being produced as the 276 nm photons were Rayleigh-scattered from the target beam, and liberating photoelectrons from the walls of the box. These electrons attached to SF_6 to give rise to a large SF_6^- background signal. At first the Ti plates (work function ϕ=4.33 eV) were gold-plated (ϕ=5.1 eV) to raise the work function of the nulling surfaces to a value above the energy of the 276 nm radiation (ϕ=4.49 eV). While this served to eliminate the background completely, we were unable to achieve better than 1 meV resolution, presumably due to strong patch fields at the Au surface. All solid surfaces were then replaced with a six-sided enclosure of pure, 92%-transmitting tungsten mesh mounted on a thin stainless-steel frame. Independent voltages could be placed on each face. Dimensions of the frame were 5.8×9.7×9.7 cm. This eliminated the surface photoelectrons, and allowed for sub-meV resolution.

Any residual background of SF_6^- arising from the 276 nm photon beam scattering from other surfaces was corrected by detuning the time delay between the pulsed tripling jet and the laser pulse. In this way, the 92 nm photons were eliminated, and the 276 nm background alone measured. Typically, this correction was less than 0.5 Hz. It was also verified that this background was featureless over the range $0 \leq \epsilon \leq 130$ meV.

A critical challenge to eliminating small electric fields is the actual measurement of the fields themselves. Two separate techniques were used. In one we measured the Stark splitting in the Xe Rydberg states, and in the second we gauged the energy width of the SF_6 attachment threshold. The monitoring of Stark splitting takes advantage of the fragility of Rydberg atoms in electric fields. When tuned below the $^2P^\circ_{1/2}$ ionization threshold, the VUV laser excites autoionizing levels in the $nd'[3/2]^0_1$

Rydberg series (the levels used for wavelength calibration). Any residual electric field within the attachment region will cause Stark-splitting of the m_l sublevels. Since the $nd'[3/2]^0_1$ levels have broad resonance widths, Stark splitting manifests itself as increased broadening of the resonances. For large enough electric field $\mathscr{E}$, the splitting will be comparable to the spacing between n-levels, hence individual n-levels will be blended. The field strength at which blending occurs, and where l-mixing of the n-levels becomes efficient, is approximated by the Inglis-Teller limit. This value is given as $\mathscr{E} = 1.71 \times 10^{12}\, n^{-5}$ mV/cm [33]. The laser linewidth (here, 0.3 cm^{-1}) limits the highest resolvable n-level to approximately 80. Since we are able to resolve states at n=80, the Inglis-Teller limit to the residual field is $\mathscr{E} \leq 500$ mV/cm. The residual field is further reduced by adjusting the grids bias voltages to minimize the width of the Rydberg resonances. In practice, we find it possible to minimize the resonance widths to achieve a resultant field to $\mathscr{E} \leq 5$ mV/cm. This $\mathscr{E}$ is still too large for conducting attachment experiments sub-meV energy resolution. We therefore rely on the attachment threshold itself as a more sensitive probe of residual electric field. The threshold width is dependent principally on the electron energy resolution. We thus adjust the bias voltages until the width of the attachment threshold is minimized. Analysis of the electron attachment signal (see Sec. IV) indicates that the electric field can be reduced to $\mathscr{E} \leq 1$ mV/cm.

IV. RESULTS AND DATA ANALYSIS

A. Threshold Electron Attachment

The SF_6^- signal, normalized for laser power fluctuations, is shown in Fig. 2 over the energy range $-0.8 \leq \epsilon \leq 5.2$ meV. (Negative scattering energies correspond to VUV photon energies below the $^2P^o_{1/2}$ threshold.) These data were taken using solid Ti plates as the electric-field nulling box. Additional data at these low energies, taken months later with the 92%-transmitting tungsten mesh frame, are shown in Fig. 3 for the range $-2.0 \leq \epsilon \leq 2.2$ meV. Above the $^2P^o_{1/2}$ threshold ($\epsilon = 0.0$ meV), monotonically

decreasing behavior given by *s*-wave scattering is observed.

A computational model was constructed to understand the signal just above and below threshold, as well as to establish the instrumental energy resolution. This model used a Gaussian function to represent the electron energy distribution. This distribution was convoluted with the assumed theoretical shape of the electron attachment cross section. In the present context, two forms may be taken for $\sigma_A(\epsilon)$: one is given by the Wigner *s*-wave behavior [26] $\sigma_A(\epsilon) = \sigma_o\epsilon^{-1/2}$, and the other by the Klots form [24,27] $\sigma_A(\epsilon) = \sigma_o\epsilon^{-1}[1-\exp(-\beta\epsilon^{1/2})]$. Here, σ_o is the normalization constant to the cross-section scale, and β is sometimes fixed by the SF_6 polarizability α, and sometimes treated as an adjustable parameter. The Gaussian electron-energy width is varied within both forms, and results are compared to data. The best fit for both cross sections is shown in Figs. 2 and 3 along with data. An energy width of 0.1 meV is found to best describe the data in Fig. 2, and a width of 0.5 meV provides the best fit in Fig. 3. Of the two, the results in Fig. 2 cover a broader energy range, and one sees that the Wigner cross section provides a better description of the data than does the Klots cross section. This is consistent with the data of Fig. 3, where differences appear only in the range $-0.5 \leq \epsilon \leq 0.5$ meV.

Interpretation of the threshold behavior of the attachment signal can be influenced by the negative ion signal just below threshold [see Figs. 2,3]. It would be natural to assume that the signal below threshold arises from the finite energy resolution, causing spill-over of signal from positive energies. But our model shows conclusively that the resolution-broadening cannot account for a significant portion of this signal. Rather, it must be due to charge-exchange collisions between SF_6 and long-lived Xe^* Rydberg states. As mentioned above, it is assumed that the autoionizing Rydberg members converging to the $^2P^o_{1/2}$ threshold are short-lived so that the charge-exchange signal can be ignored. However, for large principal quantum number *n* the level lifetime will become significant relative to the interaction time for a free electron (about 0.1 μs for a 10 meV electron). The charge-exchange signal may thus obscure the threshold position. Given that the autoionizing lifetime scales as n^3, the $nd'[3/2]^0_1$ series lifetime for

autoionization becomes important above n = 500, or for a binding energy below 0.05 meV. Furthermore, stray electric fields that exceed the Inglis-Teller limit cause efficient l-mixing of the low-l Xe Rydberg states reached by the laser excitation. Because of reduced channel coupling with the core, high-l states are expected to be longer lived than low-l states. For stray fields encountered in our apparatus (less than 0.5 mV/cm), we expect effective l-mixing to take place above $n = 200$, or at a binding energy below 0.34 meV.

Incorporating the n dependence for the autoionization lifetime (n^3 below the Inglis-Teller limit and n^4 above this limit) we find a good fit to data when the stray field is chosen to be 0.2 mV/cm for Fig. 2 and 1.0 mV/cm for Fig. 3. These field strengths agree well with the energy resolution measured in the positive energy regime. Note that our model appears to break down in Fig. 2 for energies within 0.1 meV of threshold. This likely originates from saturation of the experimental signal due to the large attachment cross section, and long Rydberg lifetime.

Shown in Fig. 4 is the electron attachment behavior for SF_6^- formation in the larger energy range $0.08 \le \epsilon \le 127$ meV. Here, the data were converted to attachment cross sections using the relation [19],

$$k(\bar{\epsilon}) = (2/m)^{1/2} \int \sigma_A(\epsilon) \epsilon^{1/2} f(\epsilon) d\epsilon \ , \qquad (3)$$

where $k(\bar{\epsilon})$ is the thermal electron rate constant at mean electron energy $\bar{\epsilon}$ and $f(\epsilon)$ is the Maxwellian electron energy distribution function given by,

$$f(\bar{\epsilon}) = (2/\sqrt{\pi})(3/2\bar{\epsilon})^{3/2} \epsilon^{1/2} \exp[-3\epsilon/2\bar{\epsilon}] \ . \qquad (4)$$

For either line shape the constant σ_o is obtained by integrating Eq. (1) using the experimental value for $k(\bar{\epsilon})$. This value was chosen to correspond to attachment by a cold (50K) SF_6 target, and was estimated from its temperature dependence (see Fig. 3 of Ref. [6]) as 2.7×10^{-7} cm^3/s . We point out

that values of $(\bar{\epsilon})$ at other T may be used in the normalization integral Eq. (3). The expressions for the attachment cross sections in the Wigner and Klots forms then become, for $\sigma_A(\epsilon)$ in cm^2 and ϵ in eV,

Wigner: $$\sigma_A(\epsilon) = 4.54 \times 10^{-15}\ \epsilon^{-1/2} \quad \textbf{(5)}$$

Klots: $$\sigma_A(\epsilon) = 5.38 \times 10^{-16}\, \epsilon^{-1}\, [1-\exp(-12.807\ \epsilon^{1/2})] \quad \textbf{(6)}$$

Plotted in Fig. 4 is the Wigner *s*-wave form, Eq. (5). Also plotted are three Klots forms with the exponential factor 12.807, corresponding to β=0.405 [23]; the factor 7.210, corresponding β=0.228 and the accepted polarizability of 44.1 a_o^3 for SF_6; and the factor 2.530 corresponding to β=0.08. The present data are fit best by the Wigner form, or a Klots form with small β (a near *s*-wave description).

B. Vibrational Excitation

New experimental and theoretical work has been carried out on vibrational excitation of SF_6 and CH_3I at these ultralow electron energies [12,14,24]. Where the combined long-range dipole and polarizability potentials are strong enough, one may have temporary capture of the electron in the potential of the excited vibrational level. These so-called Feshbach resonances are characterized by a small positive electron affinity in the excited state; and by peaks in the attachment cross section at an energy *lower* than the spectroscopic threshold (see, for example, Fig. 1 of Ref. [14]). Theoretically, true Feshbach resonances are found by searching for zeros in the determinant of the inverted *S*-matrix, at energies close to each vibrational threshold [12,14]. In other non-bound cases, one may *still* observe a discontinuity in the slope ("cusp") at the opening of a new vibrational-excitation channel. This discontinuity is generally located at or near the energy of the spectroscopic threshold. It may also exhibit a variety of shapes; *i.e.*, the drop in cross section can occur at an energy either slightly *above* or slightly *below* the threshold.

In SF_6, two vibrational resonances have been previously observed in the electron attachment spectrum that correspond to the ω_1 and ω_3 vibrational modes at 97.1 and 117.6 meV, respectively

[22,23]. A tenuous feature has also been detected, corresponding to the ω_6 mode [34]. Its energy is is known to be 43.2±0.4 meV from optical spectroscopy [35]. In the present study we examined the three regions near the ω_1 , ω_3 , and ω_6 vibrational modes of SF_6. There were clearly-observed enhancements in the attachment at electron energies near these modes. Shown in Fig. 5 is the ω_6 cusp, and cusps associated with the ω_1 and the ω_3 modes. The tungsten mesh cage was used in these measurements. This allowed for reduced and more uniform patch fields, a higher surface work function, and an unobstructed expansion of the target beam with a minimum of heating *via* gas-wall reflections. The ω_6 mode was clearly detected with both the solid titanium cage and the tungsten mesh cage. All data presented herein were taken with a pulsed, supersonic mixture of Xe and SF_6.

A surprising behavior of this feature, and one not observed in earlier results [34], is the fact that the peak of the ω_6 mode is shifted away from its spectroscopic threshold towards higher energies, by approximately 3 meV. The presence of a Feshbach resonance would result in a shift to lower energies, while the more usual cusp enhancements, as detected in the ω_1 and ω_3 channels, appear to have line shapes centered at their spectroscopic thresholds. It appears that the interference between the direct *s*-wave attachment and vibrational excitation results in a pattern where there is a flattening or slight dip at 43 meV, with a peak at 46 meV. However, there is no explanation for this shift in the ω_6 mode. The possibility was examined wherein one could have a shape resonance associated with the ω_6 mode. One can calculate the angular momentum barrier for an *l*-wave attachment process by expressing the effective potential $U_{eff}(r)$ of the electron-molecule interaction as the sum of a repulsive angular momentum term and attractive polarization as (in atomic units),

$$U_{eff}(r) = \frac{l(l+1)}{2r^2} - \frac{\alpha}{2r^4} . \qquad (7)$$

Here l is the angular momentum of the incident electron, r is the electron-molecule distance, and α is the polarizability of SF_6, taken here as 44.1 a_o^3 [36]. Simple calculation shows that there is a maximum in

this potential, at $r_{max}^2 = 2\alpha / l(l+1)$, of magnitude $U_{eff}(r_{max}) = l^2(l+1)^2 / 8\alpha$. Values r_{max} and $U_{eff}(r_{max})$ are 6.6 a_o and 309 meV for an entering *p*-wave; and 3.8 a_o and 2777 meV for an entering *d*-wave. From the magnitude of the barrier heights one concludes that (barring some anomalous increase of α in the excited ω_6 mode) non-*s*-wave states will be effectively excluded from the inner molecular attachment region, and that a shape resonance at these low electron energies is improbable.

Another possibility is that a combination band is excited by the 43-46 meV electron. Combination bands in this energy region are $2\omega_5$-$2\omega_6$ (44.0 meV), $\omega_4+\omega_5-\omega_1$ (44.4 meV), $\omega_1+\omega_5-\omega_3$ (44.6 meV), $\omega_2+\omega_5-\omega_1$ (47.8 meV), and $\omega_3-\omega_5$ (52.5 meV). This cause again seems unlikely, as one would expect combination bands to be weaker than the fundamental bands, since anharmonicities are small for vibrations occurring near the minimum of the SF_6 potential well.

V. CONCLUSIONS

The energy dependence of the electron attachment cross section for SF_6 is measured at electron energies in the range $-0.8 \leq \epsilon \leq 127$ meV. A computational model indicates that sub-meV resolution is achieved, and that the attachment cross section is better described by the Wigner *s*-wave threshold behavior, rather than the Klots parametrized form, at energies $\epsilon \leq 5$ meV. For most of the energy range herein, present data are best described by the pure *s*-wave form, or a Klots form with small β.

Vibrational enhancement or cusps have been clearly detected in the ω_6, ω_1, and ω_3 vibrational modes. While the location of the ω_1 and ω_3 cusps are near their spectroscopic energies, there is an unexplained shift in the lowest-energy ω_6 cusp, to an energy 3 meV higher than its spectroscopic value.

ACKNOWLEDGMENTS

We thank I. Fabrikant, H. Hotop, and W. Domcke for helpful correspondence. We also thank V. Garkanian for technical assistance. This work was sponsored by the AMOP Offfice of the National Science Foundation, and was carried out at the Jet Propulsion Laboratory, California Institute of Technology, through agreement with the National Aeronautics and Space Administration.

References

[1] L. G. Christophorou and J. K. Olthoff, J. Phys. Chem. Ref. Data. **29**, 267 (2000).

[2] M. Külz, M. Keil, A. Kortyna, B. Schellhaaß, J. Hauck, K. Bergmann, W. Meyer and D. Weyh, Phys. Rev. A **53**, 3324 (1996).

[3] A. Chutjian and J. M. Ajello, J. Chem. Phys. **66**, 4544 (1977).

[4] F. B. Dunning, J. Phys. B **28**, 1645 (1995).

[5] A. Chutjian, A. Garscadden and J. M. Wadehra, Phys. Reports **264**, 393 (1996).

[6] O. J. Orient and A. Chutjian, Phys. Rev. A **34**, 1841 (1986).

[7] O. J. Orient, A. Chutjian, R. W. Crompton, and B. Cheung, Phys. Rev. A **39**, 4494 (1989).

[8] T. F. O'Malley, Phys. Rev. **150,** 14 (1966).

[9] J. P. Gauyacq and A. Herzenberg, J. Phys. B **17**, 1155 (1984).

[10] I. I. Fabrikant, Phys. Rev. A **43**, 3478 (1991).

[11] I. I. Fabrikant, Comm. At. Mol. Phys. **32**, 267 (1996).

[12] A. Schramm, I. I. Fabrikant, J. M. Weber, E. Leber, M-W. Ruf, and H. Hotop, J. Phys B **32**, 2153 (1999).

[13] I. I. Fabrikant, in *The Physics of Electronic and Atomic Collisions* (ed. Y. Itikawa, K. Okuno, H. Tanaka, A. Yagishita, and M. Matsuzawa, CP500, AIP, New York, 2000).

[14] H. R. Sadeghpour, J. L. Bohn, M. J. Cavagnero, B. D. Esry, I. I. Fabrikant, J. H. Macek, and A. R. P. Rau, J. Phys. B **33**, R93 (2000).

[15] B. G. Zollars, C. Higgs, F. Lu, C. W. Walter, L. G. Gray, K. A. Smith, F. B. Dunning, and R. F. Stebbings, Phys. Rev. A **32**, 3330 (1985).

[16] X. Ling, B. G. Lindsay, K. A. Smith, and F. B. Dunning, Phys. Rev. A **45**, 242 (1992).

[17] M. T. Frey, S. B. Hill, K. A. Smith, F. B. Dunning, and I. I. Fabrikant, Phys. Rev. Letters **75**, 810 (1995).

[18] A. Chutjian, Phys. Rev. Lett. **46**, 1511 (1981).

[19] A. Chutjian and S. H. Alajajian, Phys. Rev. A **31**, 2885 (1985).

[20] A . Chutjian and S. H. Alajajian, Phys. Rev. A **35**, 4512 (1987).

[21] S. H. Alajajian and A. Chutjian, Phys. Rev. A **37**, 3680 (1988); A. Chutjian, S. H. Alajajian, and K-F. Man, Phys. Rev. A **41**, 1311 (1990).

[22] D. Klar, M.-W. Ruf, and H. Hotop, Chem. Phys. Lett. **189**, 448 (1992).

[23] D. Klar, M-W. Ruf, and H. Hotop, Aust. J. Phys. **45**, 263 (1992).

[24] D. Klar, M-W. Ruf, and H. Hotop, Meas. Sci. Technol. **5**, 1248 (1994).

[25] A. Schramm, J. M. Weber, J. Kreil, D. Klar, M-W. Ruf, and H. Hotop, Phys. Rev. Letters **81**, 778 (1998).

[26] E. P. Wigner, Phys. Rev. **73**, 1002 (1948).

[27] C. E. Klots, Chem. Phys. Lett. **38**, 61 (1976).

[28] A. Kortyna, M. Durrach, P-T. Howe, and A. Chutjian, J. Opt. Soc. Am. B **17**, 1934 (2000).

[29] R. Falcone and J. Bokor, Opt. Let. **8**, 21 (1983).

[30] K. Yoshino and D. Freeman, J. Opt. Soc. Am. B **2**, 1268 (1985).

[31] J. A. R. Samson, in *Adv. Atom. Molec. Physics* (Academic, New York, 1966), v. 12, p.177.

[32] M. T. Frey, L. Ling, B. G. Lindsay, K. A. Smith, and F. B. Dunning, Rev. Sci. Instrum. **64**, 3649 (1993).

[33] W. A. Chupka, J. Chem. Phys. **98**, 4520 (1993); F. Merkt, H. H. Fielding, and T. P. Softley, Chem. Phys. Let. **202**, 153 (1993).

[34] E. Leber, J. M. Weber, A. Gopalan, M.-W. Ruf and H. Hotop, Proc. 6th European Conf. Atom. Molec. Phys. (Siena, Italy, 1998)(unpublished).

[35] D. Bermejo, R. Z. Martínez, E. Loubignac, V. Boudon and G. Pierre, J. Molec. Spectrosc. **201**, 164 (2000); V. Boudon, M. Hepp, M. Herman, I. Pak, and G. Pierre, J. Molec. Spectrosc. **192**, 359 (1998); R. S. McDowell, B. J. Krohn, H. Flicker, and M. C. Vasquez, Spectrochim. Acta **42A**, 351 (1986); R. S. McDowell and B. J. Krohn, Spectrochim. Acta **42A**, 371 (1986); R., S. McDowell, J. P. Aldridge, and R. F. Holland, J. Phys. Chem. **80**, 1203 (1976); W. F. Brooks, M. Eshaque, C. Lau, and J. Passmore, Can. J. Chem. **54**, 817 (19786).

[36] R. D. Nelson, Jr. and R. H. Cole, J. Chem. Phys. **43**, 4033 (1971).

Figure Captions

Figure 1 Schematic diagram of the laser photoionization apparatus. The legend is: **Nd:YAG** - 10 Hz pulsed Nd:YAG laser; **DX** - doubling crystal; **DyL** - dye laser; **MX** - mixing crystal; **QL** - quartz focusing lens; **TC** - tripling chamber; **T** - frequency-tripling pulsed jet (Xe); **TMP1** - 250 ℓ/s turbomolecular pump; **B** - differential pumping baffle; **DBS** - dichroic beam splitters; **IR** - negative ion rejection sleeve; **PM** - power meter to measure 276 nm power; **NB** - electric-field nulling box; **G** - SF_6/Xe target beam; **EC** - ion extraction cone; **IL** - ion focusing lens system; **P** - pulsed voltage on EC and first lens element; **QMS** - quadrupole mass spectrometer; **CEM** - channel-type electron multiplier; **PA** - pulse preamplifier; **TMP2** - 250 ℓ/s turbomolecular pump; **PC** - personal computer; **MC** - master clock to control data acquisition and voltage pulses to elements **T**, **G**, and **P**.

Figure 2 Details of the electron attachment signal in the energy range $-0.8 \leq \epsilon \leq 5.2$ meV. Shown are calculated line shapes assuming the Wigner cross section (solid line) and the Klots cross section (dashed line) with β=0.405 (ϵ in meV). An electron energy distribution of width 0.1 meV (FWHM) and a stray field of 0.2 mV/cm are assumed in the fitting. The wavelength scale is calibrated here and elsewhere to 0.1 meV.

Figure 3 Details of the electron attachment signal in the energy range $-2.0 \leq \epsilon \leq 2.2$ meV. Shown are calculated line shapes assuming the Wigner cross section (solid line) and the Klots cross section (dashed line) with β=0.40 (ϵ in meV). An electron energy distribution of width 0.5 meV (FWHM) and a stray field of 1.0 mV/cm are assumed in the fitting.

Figure 4 Cross section for electron attachment to SF_6 over the energy range $0.08 \leq \epsilon \leq 127$ meV. Experimental data are shown as solid circles. Solid line is the Wigner *s*-wave cross section form given by $\sigma_A(\epsilon) = 4.54 \times 10^{-15}\ \epsilon^{-1/2}$ cm^2 for attachment to a cool (~50K) SF_6 target. Short-dashed line (----) is a best fit to the data using the Klots form with β=0.08 (ϵ in meV), chain curve (– · – · –) is the fit β=0.228 (corresponding to the polarizability for SF_6 of 44.1 a_o^3), and long dashed line (– – – –) are data from Ref. [23] using the Klots form with β=0.405. Arrows indicate the vibrational enhancement cusps (see Fig. 5).

Figure 5 Electron attachment to SF_6 showing vibrational enhancements in the ω_6, ω_1, and ω_3 vibrational modes. Arrows in each case indicate the spectroscopic energies, as summarized in Ref. [35].

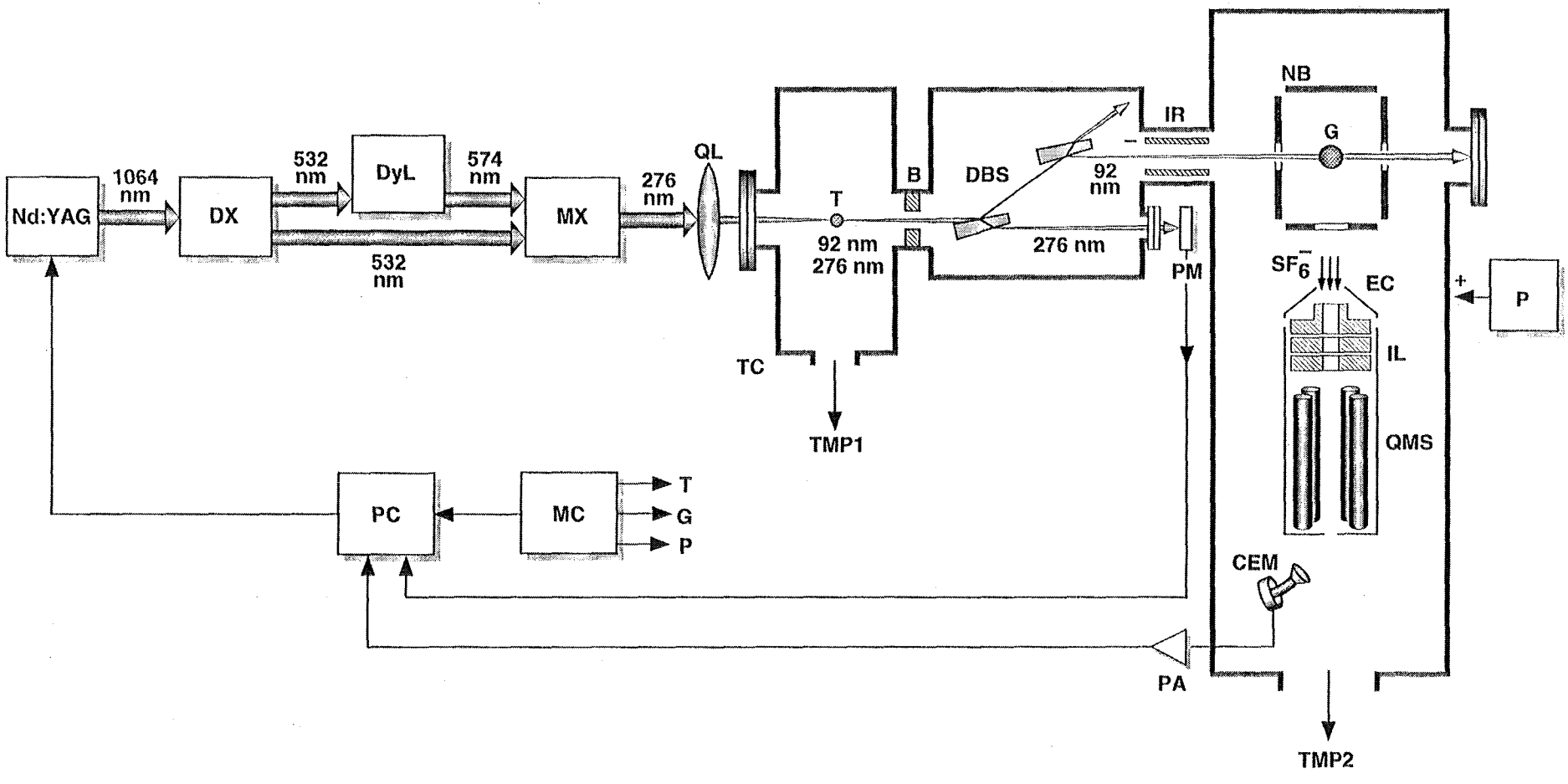
Nd:YAG
1064 nm
DX
532 nm
DyL
574 nm
532 nm
MX
276 nm
QL
T
92 nm
276 nm
B
DBS
92 nm
276 nm
IR
NB
G
PM
SF6
EC
IL
QMS
P
TC
TMP1
PC
MC
T
G
P
CEM
PA
TMP2

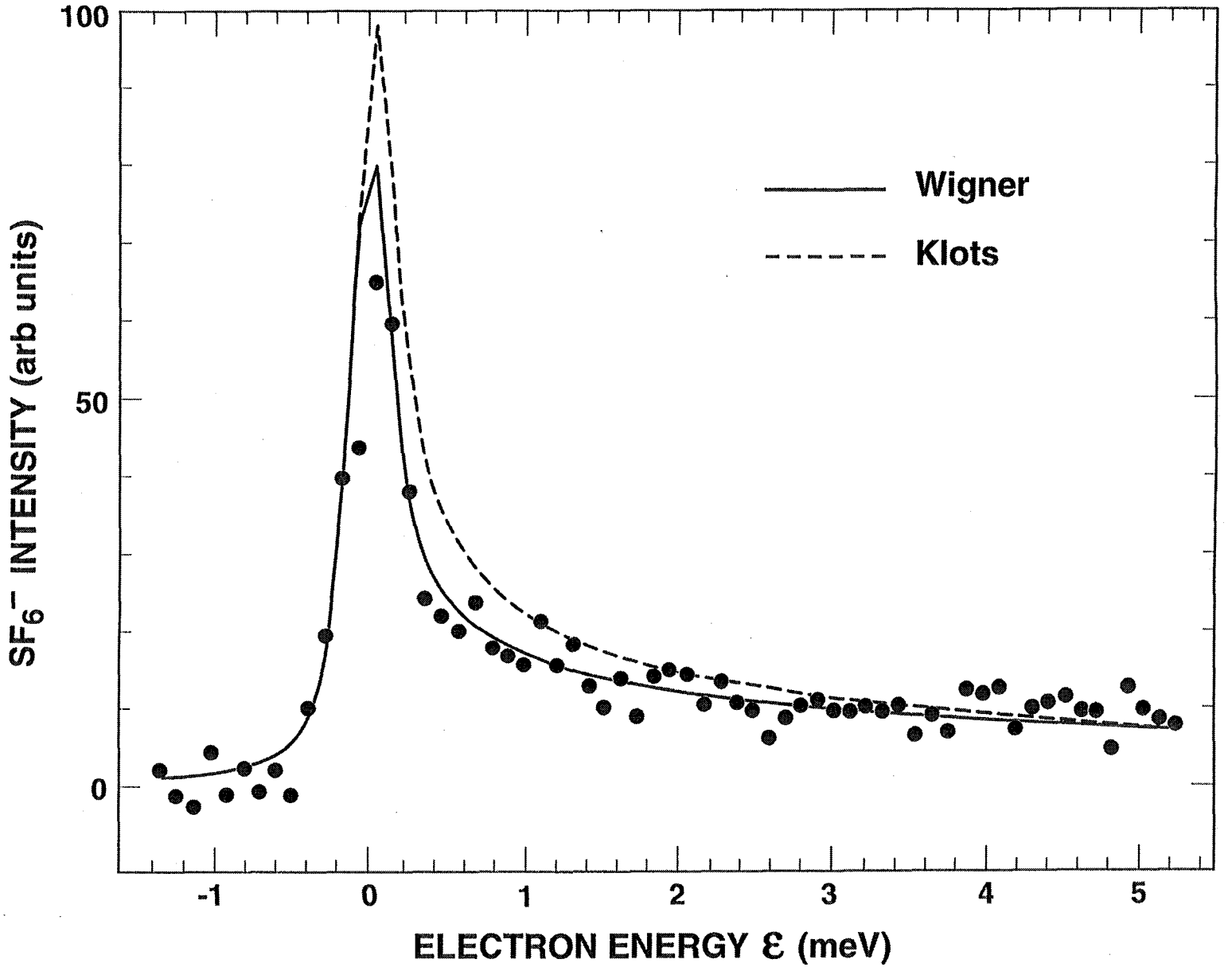
100
50
0
SF_6^- INTENSITY (arb units)
Wigner
Klots
-1
0
1
2
3
4
5
ELECTRON ENERGY ε (meV)

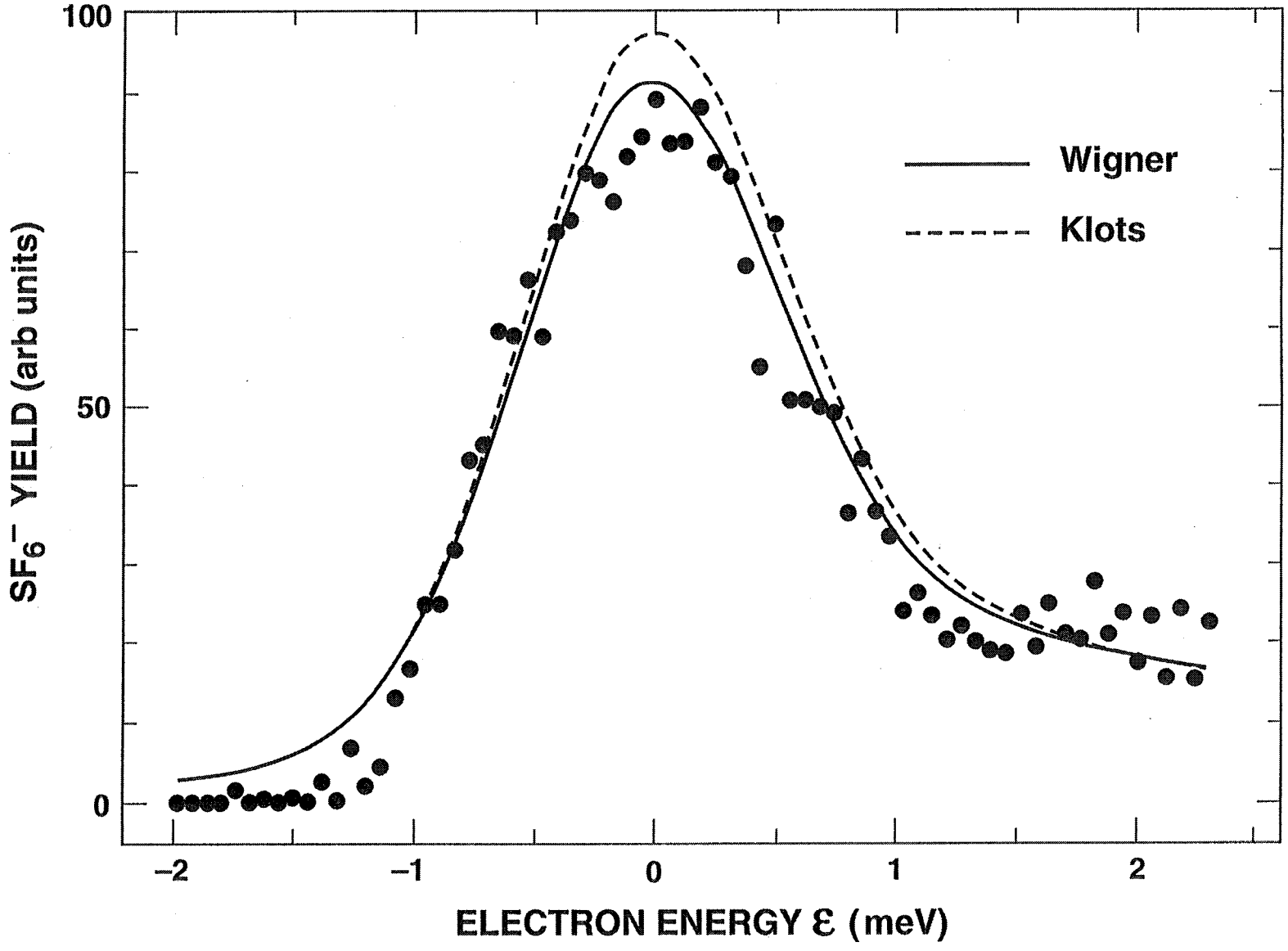
100
50
0
SF_6^- YIELD (arb units)
Wigner
Klots
–2
–1
0
1
2
ELECTRON ENERGY ε (meV)

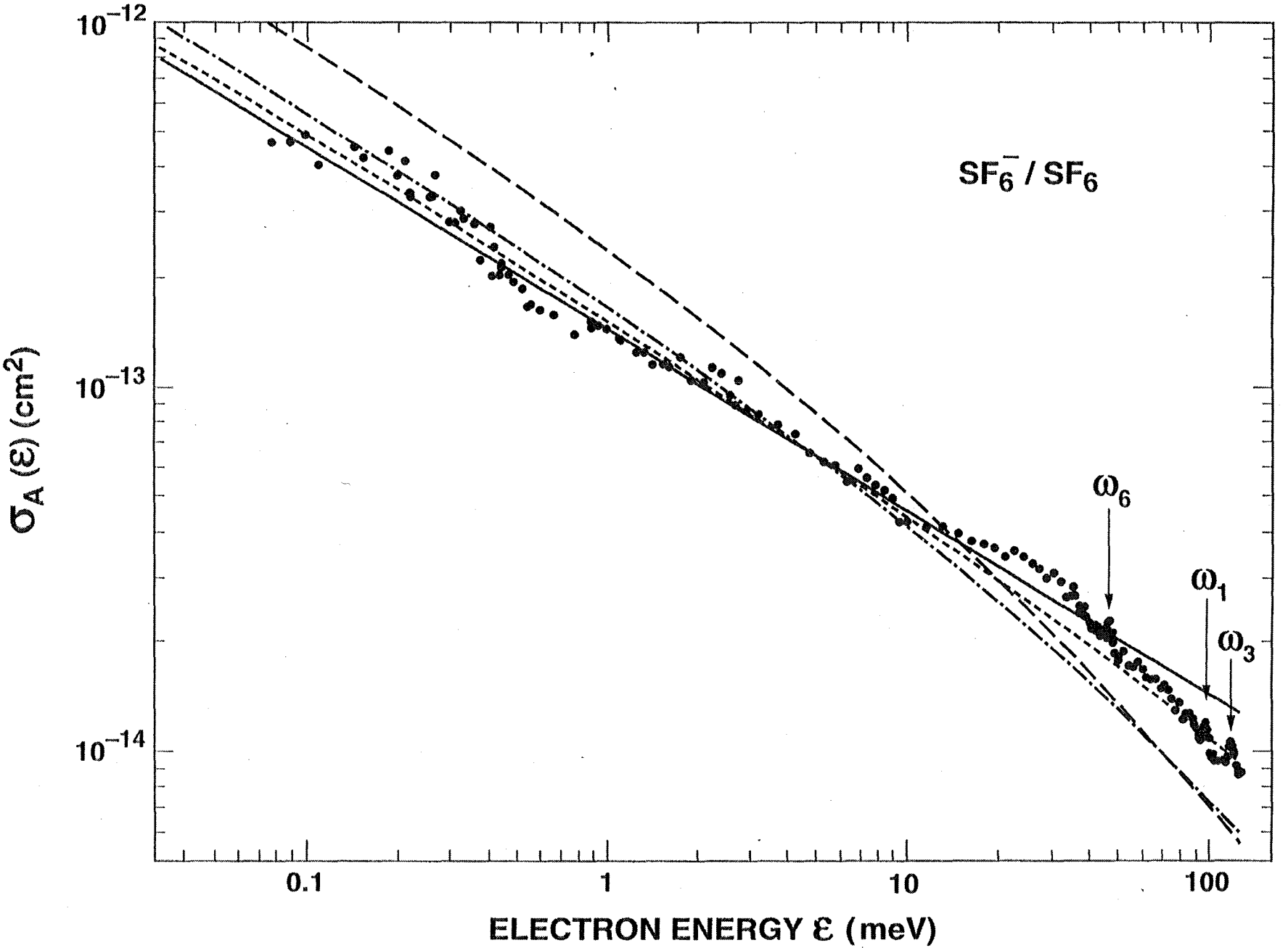
10^{-12}
10^{-13}
10^{-14}
$\sigma_A(\varepsilon)$ (cm^2)
SF_6^- / SF_6
ω_6
ω_1
ω_3
0.1
1
10
100
ELECTRON ENERGY ε (meV)

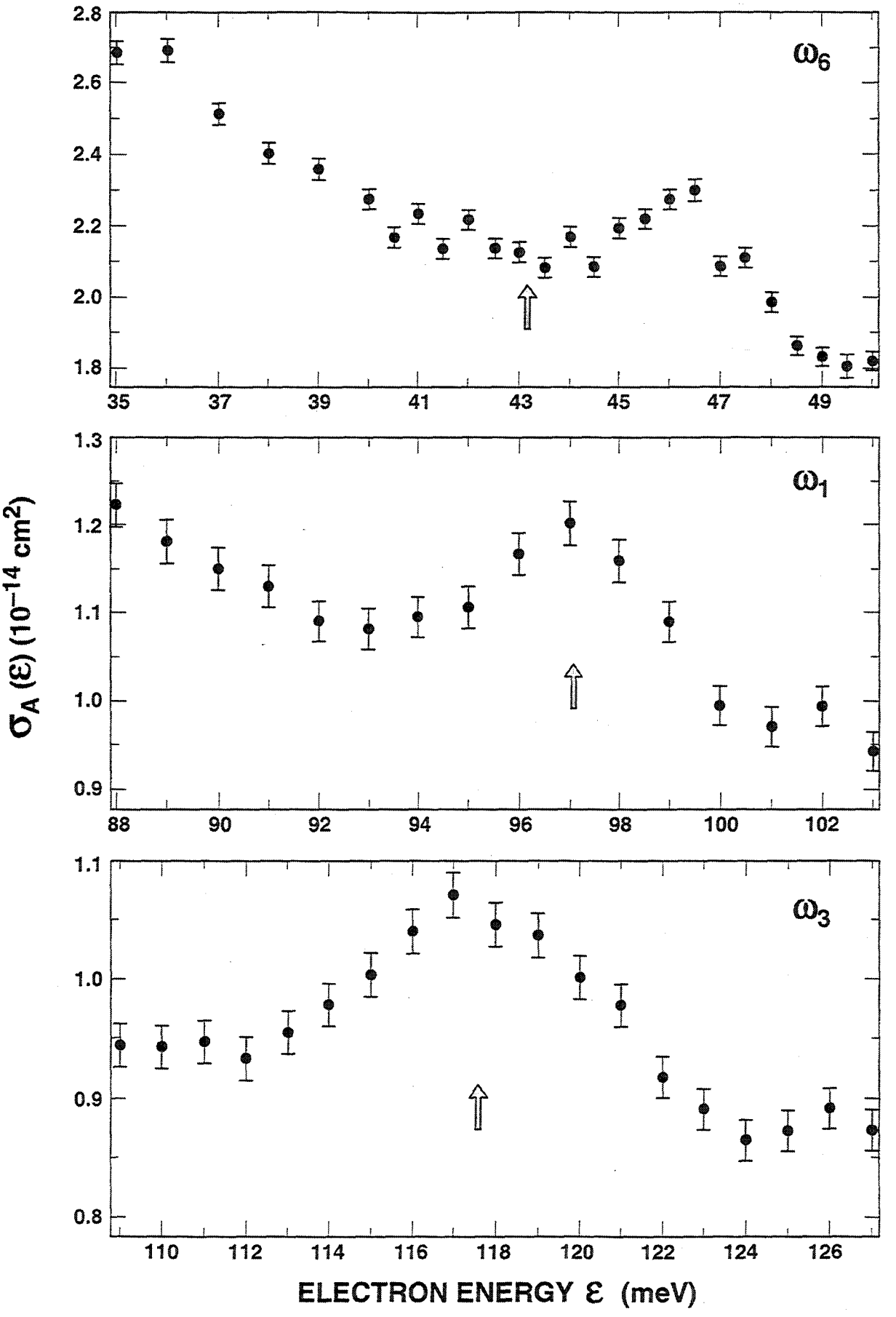
ω_6
ω_1
ω_3
$\sigma_A(\mathcal{E})$ $(10^{-14}\,cm^2)$
ELECTRON ENERGY $\mathcal{E}$ (meV)